

# Effect of Emitting Electrode Number on the Performance of EHD Gas Pump in a Rectangular Channel

J. Zhang and F. C. Lai

School of Aerospace and Mechanical Engineering

University of Oklahoma

phone: (1) 405-325-1748

e-mail: flai@ou.edu

**Abstract**—Previous studies have shown that electric field in the form of corona wind can be used for gas pumping. It has also been shown that the maximal volume flow rate can be achieved by an optimal design and arrangement of electrode(s) involved. In this study, the number of emitting electrodes has been considered for its effect on the pump performance. To seek the relation between the electrode number and pump performance, an EHD gas pump with three configurations (4, 12, and 28 emitting electrodes) is critically evaluated by experimental measurements and numerical simulations.

## INTRODUCTION

It has long been known that an electrohydrodynamically (EHD) induced secondary flow (i.e., corona wind or ionic wind) can significantly enhance heat and mass transfer [1-3]. The net effect of this secondary flow, which can be thought of as a micro-jet of fluid issued from the charged electrode to the grounded surface, is additional mixing of fluids and destabilization of boundary layer, therefore leading to a substantial increase in the heat and mass transfer coefficients. Corona wind is produced by an electrode charged with a direct current (positive or negative) at a sufficiently high voltage (in the kV range). While the applied voltage may be high, the current involved is usually very small (in the  $\mu\text{A}$  to mA range), which makes the power required considerably insignificant. This has become one of the most attractive features for EHD technique. In recent years, there has been a surge of interest in the application of EHD technique for pumping dielectric liquids [4]. Because of their low power consumption and no moving part, EHD pumps have been considered a valuable alternative for conventional pumps.

Rickard, et al. [5] investigated the characteristics of ionic wind velocity in a tube with a pin-to-ring electrode geometry for negative corona discharge. In addition, they added a converging nozzle to the exit of the tube with an intention to accelerate the gas flow produced by the ionic wind generator. However, they found that only a slight increase in the velocity was achieved by using the converging nozzle. A wire-non-parallel-plate EHD

gas pump was experimentally investigated by Tsubone, et al. [6]. A maximum air velocity of 1.9 m/s, which corresponds to a volumetric flow rate of 44 L/min, was observed. The volumetric flow rate, gas velocity and pressure drop were found to increase with increasing applied voltage or EHD number. Also, their numerical results [7] agreed qualitatively well with their experimental data. The flow characteristics of a wire-rod type EHD gas pump were studied by Komeili, et al. [8] for various pipe diameters. Experiments were conducted for negative DC applied voltage ranging from 0 to 24 kV. A maximum gas flow rate of 40.1 L/min was generated for a pipe diameter of 20 mm, with a grounded rod electrode of a diameter of 3.1 mm and an electrode spacing of 12.6 mm. Their results showed that for the same pipe diameter and electrode spacing, the velocity generated increased with the rod diameter. However, they suggested that for a fixed gas velocity it was better to use a rod electrode with a smaller diameter as it would generate the same flow velocity for lower power consumption. The efficiency of an EHD gas pump with a grid-and-ring grounded electrode has been experimentally evaluated by Moreau and Touchard [9]. Their results showed that positive coronas could produce a higher air velocity than negative ones. Using a grid as the collecting electrode was more efficient than a ring. In their experiments, they were able to produce a corona wind of 10 m/s and a flow rate of about 1 L/s. Shooshtari, et al. [10] reported that the implementation of corona wind in small scales was not only feasible, but also preferable as it could lead to considerable heat transfer enhancement. It was shown that heat transfer enhancement up to 200% was attainable while the amount of EHD power was only about 1.13 W.

Although EHD gas pumps are promising, there are still some challenging questions to be addressed. The first is associated with the high voltage required to drive the flow in a large scale system. However, it is expected that the operating voltage will decrease as the scale of the system is reduced, thus promoting its wide spread use in microsystems. In fact, the implementation of EHD pumping has received tremendous attention lately due to an increasing interest in microfluidics, chip-integrated cooling, and drug delivery systems [11]. The next challenge is related to the EHD pump configuration. The efficiency of an EHD pump lies in the design of its electrodes. An appropriate configuration of the pumping system along with an optimal spacing between the electrodes ( $L$ ) and its relation to other significant dimensions must be determined. The objective of the present study is to address one of the important issues in the EHD gas pump design, specifically the number of emitting electrodes. As one may anticipate, the number of emitting electrodes will not only affect the distribution of electric field, but also complicate the interaction between corona jets issued from two neighboring electrodes. As such, the relation between the pump performance and the number of emitting electrodes becomes critical in the design of an optimal EHD pump. To aid the investigation, experimental measurements and numerical simulations have been conducted.

## EXPERIMENTAL SETUP, NUMERICAL FORMULATION AND PROCEDURE

### A. Experimental Setup

The experimental setup used in this study is shown in Fig. 1. The test channel was constructed using Plexiglas of  $\frac{1}{4}$  inch thick. The inner dimensions of the channel were 4

inches by 4 inches with a length of 20 inches. The dimensions of the wire-electrode and system configuration are shown in Fig. 2. A copper wire of 20 GA (0.03196 inch diameter) was first bent and welded to form the electrode loop. Additional one-inch-long copper wires of the same size were welded to the base loop to serve as emitting electrodes. These emitting electrodes were evenly spaced along the channel walls. Three pump configurations, separately with 4, 12, and 28 emitting electrodes, were considered in this study. A  $\frac{1}{2}$  inch wide and 0.025 inch thick copper strip, which was also mounted on all four sides of the wall, was used as the grounded plate. The gap between the tips of the emitting electrodes and the grounded plate was maintained at 1.5 inches. The electrode assembly and the grounded plate were press-fitted to pre-cut grooves on the inner wall of the channel so that their surfaces were flushed with the channel wall. In this arrangement, the corona wind produced by the electrode will resemble that of a wall jet. Also, the emitting electrodes were intended to align with the direction of primary flow to maximize its effect of pumping.

The electrode assembly was connected to a high voltage power supply (Bertan, Series 205B) and charged with a direct current of either polarity. The plate was grounded at the

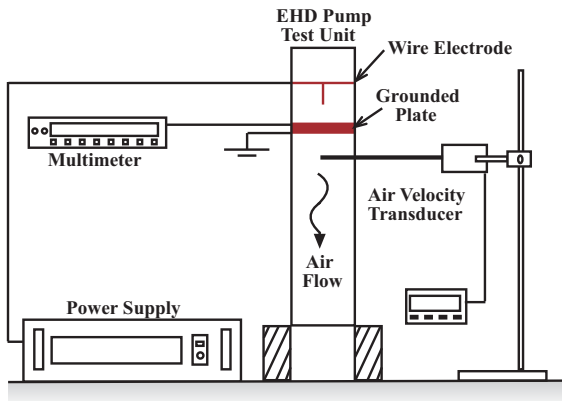


Fig. 1 Schematic of the experimental setup.

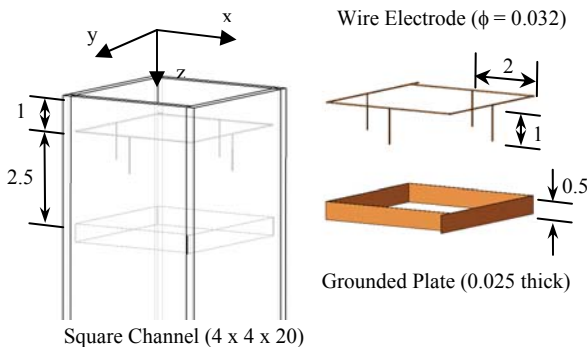


Fig. 2 An EHD gas pump with 4 emitting electrodes (dimensions in inches).

same level of the power supply. A multimeter (Fluke 8000A Series) was connected in series with the grounded plate to measure the current flowing through the ground plate. Two  $\frac{1}{4}$  inch NPT compression fittings were installed on the lower part (outlet section) of the channel to hold the velocity transducer (Omega FMA 902-I) in place to facilitate air flow measurements. The transducer, which can accurately measure air velocity from 0 to 500 fpm (2.54 m/s) with an accuracy of 2.7% of full scale at room temperature, was connected to a process meter (Omega DP 25B-E) so that the measured air velocity can be read out directly. The velocity probe extended horizontally from channel wall allowing measurements be taken on three levels; 1, 2.5 and 4 inches downstream of the grounded plate. A total of nine sampling points are evenly spaced on each level.

Prior to the start of the experiment, a spirit in glass level was used to ensure that the channel was vertically upward and that the velocity probe was horizontally leveled. To start the experiment, the applied voltage was gradually increased until a flow was detected by the velocity transducer. For the present setup, corona wind was too weak to be detected until the applied voltage was increased to 20 kV. The applied voltage was then incrementally increased by two kilovolts until sparkover occurred, which could be easily observed through a visible bright light and cracking sound that it produced. When it occurred, electric field became unstable and fluctuates violently. As such, it should be avoided to operate beyond this voltage. The V-I curve for the present experimental setup is shown in Fig. 3. As seen, the current produced by corona discharges increases with the applied voltage after the onset of corona. An EHD pump with more electrode pins produces a larger current at a given applied voltage. This trend is more pronounced at a higher voltage. The slope of V-I curve becomes steeper as the number of pins increase, particularly for the case of 28 pins with positive polarity. One also notices that, for any configuration, an EHD pump operated in positive polarity produces a higher current than that operated in negative polarity.

### B. Numerical Formulation and Procedure

For the problem considered, the governing equations for the electrical field are given by [12],

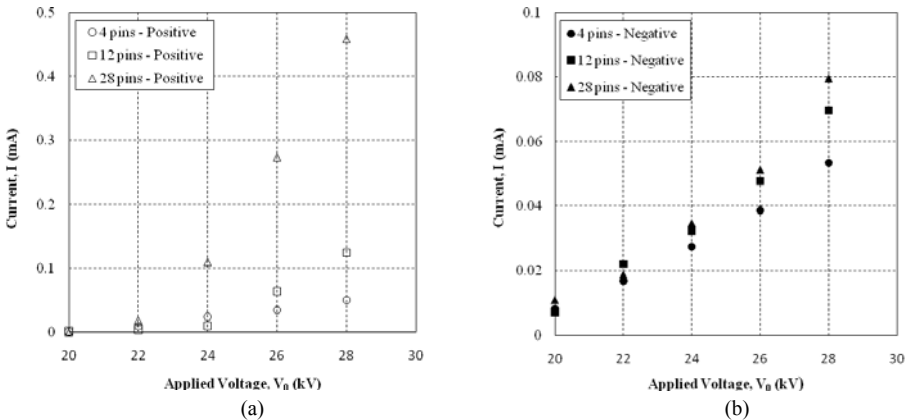


Fig. 3 V-I curve for the present experimental setup.

$$\frac{\partial^2 V}{\partial x^2} + \frac{\partial^2 V}{\partial y^2} + \frac{\partial^2 V}{\partial z^2} = -\frac{\rho_c}{\epsilon}, \quad (1)$$

$$\frac{\partial \rho_c}{\partial x} \frac{\partial V}{\partial x} + \frac{\partial \rho_c}{\partial y} \frac{\partial V}{\partial y} + \frac{\partial \rho_c}{\partial z} \frac{\partial V}{\partial z} = \frac{\rho_c^2}{\epsilon}, \quad (2)$$

which can be derived from Maxwell equation, current continuity equation and Ohm's law. The governing equations for the flow field are the continuity equation (Eq. (3)) and Navier-Stokes equations (Eqs. (4-6)), which are given below.

$$\frac{\partial u}{\partial x} + \frac{\partial v}{\partial y} + \frac{\partial w}{\partial z} = 0, \quad (3)$$

$$u \frac{\partial u}{\partial x} + v \frac{\partial u}{\partial y} + w \frac{\partial u}{\partial z} = -\frac{1}{\rho} \frac{\partial p}{\partial x} + \nu \left[ \frac{\partial^2 u}{\partial x^2} + \frac{\partial^2 u}{\partial y^2} + \frac{\partial^2 u}{\partial z^2} \right] + \frac{\rho_c}{\rho} E_x, \quad (4)$$

$$u \frac{\partial v}{\partial x} + v \frac{\partial v}{\partial y} + w \frac{\partial v}{\partial z} = -\frac{1}{\rho} \frac{\partial p}{\partial y} + \nu \left[ \frac{\partial^2 v}{\partial x^2} + \frac{\partial^2 v}{\partial y^2} + \frac{\partial^2 v}{\partial z^2} \right] + \frac{\rho_c}{\rho} E_y, \quad (5)$$

$$u \frac{\partial w}{\partial x} + v \frac{\partial w}{\partial y} + w \frac{\partial w}{\partial z} = -\frac{1}{\rho} \frac{\partial p}{\partial z} + \nu \left[ \frac{\partial^2 w}{\partial x^2} + \frac{\partial^2 w}{\partial y^2} + \frac{\partial^2 w}{\partial z^2} \right] + \frac{\rho_c}{\rho} E_z. \quad (6)$$

The last terms on the right-hand side of Navier-Stokes equations (Eqs. (4-6)) are the body forces produced by the electric field. Owing to the symmetry of the problem, only one quarter of the channel was needed for computations. Thus, the corresponding boundary conditions for the electric field are,

$$\text{At the wire,} \quad V = V_0. \quad (7a)$$

$$\text{At the grounded plate,} \quad V = 0. \quad (7b)$$

$$\text{At the inlet and outlet,} \quad \frac{\partial V}{\partial z} = 0 \quad (7c)$$

$$\text{On the channel walls except the grounded plate,} \quad x = 0, \quad \frac{\partial V}{\partial x} = 0. \quad (7d)$$

$$y = 0, \quad \frac{\partial V}{\partial y} = 0. \quad (7e)$$

$$\text{On the symmetric surfaces,} \quad x = \frac{D}{2}, \quad \frac{\partial V}{\partial x} = 0. \quad (7f)$$

$$y = \frac{D}{2}, \quad \frac{\partial V}{\partial y} = 0. \quad (7g)$$

Similarly, the boundary conditions for the flow fields are given by

$$\text{At the inlet and outlet,} \quad p = p_{\text{atm}}, \quad \frac{\partial u}{\partial z} = 0, \quad \frac{\partial v}{\partial z} = 0, \quad \frac{\partial w}{\partial z} = 0. \quad (8a)$$

$$\text{On the channel walls,} \quad x = 0, \quad u = 0, \quad v = 0, \quad w = 0. \quad (8b)$$

$$y = 0, \quad u = 0, \quad v = 0, \quad w = 0. \quad (8c)$$

$$\text{On the symmetric surfaces, } \quad x = \frac{D}{2}, \quad u = 0, \quad \frac{\partial v}{\partial x} = 0, \quad \frac{\partial w}{\partial x} = 0. \quad (8d)$$

$$y = \frac{D}{2}, \quad \frac{\partial u}{\partial y} = 0, \quad v = 0, \quad \frac{\partial w}{\partial y} = 0. \quad (8e)$$

Computations for the electric field have been performed using an in-house program based on the finite different method. Since the radius of the electrode wire is very small, it is appropriate to treat the wire as a nodal point. A uniform grid (51 x 51 x 176) has been used for the present calculations. A further refinement of grid to 81 x 81 x 256 does not produce much improvement over the results but significantly increase the computational time. For the solution of electric field, a numerical procedure proposed by Yamamoto and Velkoff [13] has been employed. In this procedure, electric potential and space charge density are determined by iterations on Eqs. (1) and (2) with an assumed value of space charge density at the wire ( $\rho_{c0}$ ). The validity of the solution is checked by comparing the predicted total current (Eq. (9)) with the measured current at the corresponding voltage. If the currents do not match, a new value of space charge density at the wire is assumed and the calculations are repeated. There are other algorithms for the solution of electric field (e.g., those proposed by McDonald et al. [14] as well as Kalio and Stock [15]), in which the electrical field condition at the wire is estimated by the Peek's semi-empirical formula [16] instead of an assumed value. It should be pointed out that an empirical constant, named the wire condition factor, has been introduced in the formula mentioned above such that the accuracy of the converged solution really depends on the value of the wire condition factor assigned. Since the assignment of this empirical constant is somewhat arbitrary, we prefer the approach proposed by Yamamoto and Velkoff [13] over the later ones [14-15]. However, it has been reported [17-18] that the agreement between the results obtained by these two approaches is very good when the solutions converged.

$$I_{\text{cal}} = 2 \int_0^D \int_0^W \rho_c b E_x \, dydz + 2 \int_0^D \int_0^W \rho_c b E_y \, dx dz, \quad (9)$$

When this calculated current agrees well with the experimental data (i.e., to satisfy Eq. (10)), the electric field is considered converged.

$$\left| \frac{I_{\text{cal}} - I_{\text{exp}}}{I_{\text{cal}}} \right| \leq 10^{-3}. \quad (10)$$

On the other hand, computations for the flow field have been performed using a commercial code FLUENT 6.3.26. After the solution of the electric field converges, electric body forces can be determined and this information is passed on to FLUENT using its user defined function. A non-uniform grid has been used for the calculations of the flow field. Finer meshes are applied to the region near the wall where the viscous and electric body forces dominate. Relatively coarse meshes are used in the regions far away from the wall and far downstream. A total of 676,000 cells have been used for the computation of flow field. Again, further refinements of the mesh do not appear to produce any significant change in the results, but merely increase the computational time tremendously. All

computations have been performed on a 64-bit workstation with 2 GHz CPU and 8 Gb RAM. A typical run takes about seven hours of CPU time for the solution of the electric field. However, the time required to solve for the flow field ranges from three hours to six hours, depending on the electrode configuration (i.e., the number of emitting electrodes) and voltage applied.

## RESULTS AND DISCUSSION

The electric potential distributions inside the channel are shown in Fig. 5 for three electrode configurations at an applied voltage of 24 kV. The potentials displayed have been normalized with the voltage applied at the wire. It is observed that a large potential gradient occurs between the wire electrode and the grounded plate. Below the grounded plate, the potential gradually decreases toward the end of the channel. From Fig. 5, one can see that the electrode pins disturb the electric field which would otherwise be uniformly stratified. This high potential gradient (i.e., high electric field intensity) is an essential condition for the generation of corona wind. Therefore, it is important to include electrode pins to create corona wind in the square channel.

To better visualize the electric field in three-dimensional space, the distributions of electric potential are displayed at various cross-sections along the channel length (i.e., X-Y plane) in Fig. 6. At the cross-section on the wire-loop ( $\bar{z} = 1/4$ ), the contour lines of electric potentials are nearly concentric with the channel wall for all configurations. This concentric pattern is disrupted by the presence of the electrode pins. The influence of the electrode pins can be clearly seen from the cross-section at the electrode tip ( $\bar{z} = 1/2$ ). As the number of pins increases, the radius of influence from each pin decreases. It is also noticed that at this level, the configuration with 4 electrode pins has the lowest potential gradient. The disturbance is still clearly visible at the level midway between the electrode tips and the grounded plate ( $\bar{z} = 11/16$ ) for the configuration with 4 electrode pins. However, with 28 electrode pins, the electric potential distribution becomes completely uniform at this level. As such, no contour line is observed. As they approach the grounded plate, the electric potential distributions become concentric again as seen from the cross-sections at the top ( $\bar{z} = 7/8$ ) and bottom edges ( $\bar{z} = 1$ ) of the grounded plate.

Space charge density distributions are shown in Fig. 7 for three electrode configurations at an applied voltage of 24 kV. The charge density displayed is also normalized with its value at the electrode tips. As observed, space charges are formed near the electrode tips and extended downwards to the grounded plate. For the configuration with 4 electrode pins, space charges are highly clustered around the electrode tips, and its density reduces dramatically within a short distance away from the tips. However, as the number of the electrode pins increases, space charges spread and extend over the region between the electrode tips and the grounded plate.

Figure 8 illustrates the space charge density distributions at various cross-sections along the channel length for three electrode configurations at an applied voltage of 24 kV. There is no space charge at the cross-section on the wire-loop level ( $\bar{z} = 1/4$ ) since space charge propagates like a wave from the electrode tips towards the grounded plate.

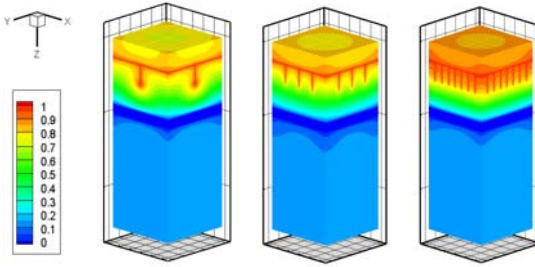


Fig. 5 Potential distribution in the channel 24 kV ( $\Delta \bar{V} = 0.05$ ), (a) 4 electrode pins, (b) 12 electrode pins, (c) 28 electrode pins.

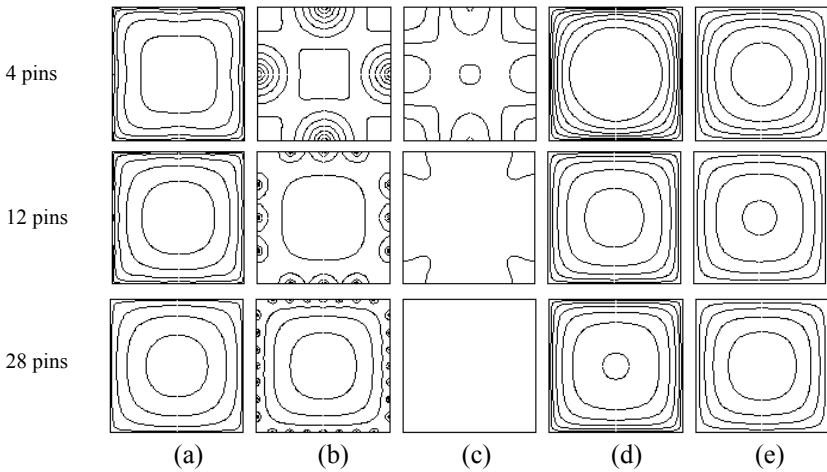


Fig. 6 Potential distribution at various cross-sections, 24 kV, ( $\Delta \bar{V} = 0.05$ )  
 (a)  $\bar{z}=1/4$ ; (b)  $\bar{z}=1/2$ ; (c)  $\bar{z}=11/16$ ; (d)  $\bar{z}=7/8$ ; (e)  $\bar{z}=1$ .

Near the electrode tips, space charges are confined to a region within a small radial distance from the tip, as seen from the cross-section  $\bar{z} = 1/2$ . At a cross-section downstream of the electrode tips ( $\bar{z} = 11/16$ ), space charge density decreases and spreads towards the center of the channel. For the configuration with 4 electrode pins, the charge density is too weak ( $\Delta \rho_c < 0.05$ ) to show on the contour plots. Although the charge density decreases as it approaches the grounded plate, the space charge field seems to be the strongest for the configuration with 12 electrode pins than that with 28 electrode pins, as seen from cross-sections of  $\bar{z} = 11/16$  and  $\bar{z} = 7/8$ . No space charge can be found below the level of the grounded plate.

Figure 9 shows the velocity profile inside the channel from both experimental results and numerical simulations for the configuration with 12 electrode pins. The velocity profiles in the other two configurations show similar characteristics. The x axis repre

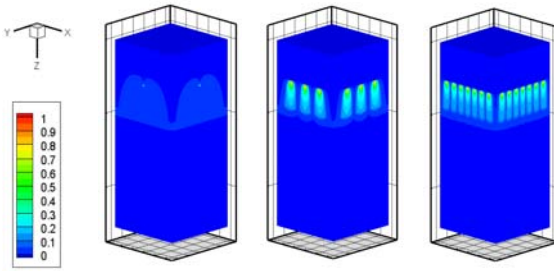


Fig. 7 Space charge distribution in the channel 24 kV ( $\overline{\Delta\rho_c} = 0.05$ ), (a) 4 electrode pins, (b) 12 electrode pins, (c) 28 electrode pins.

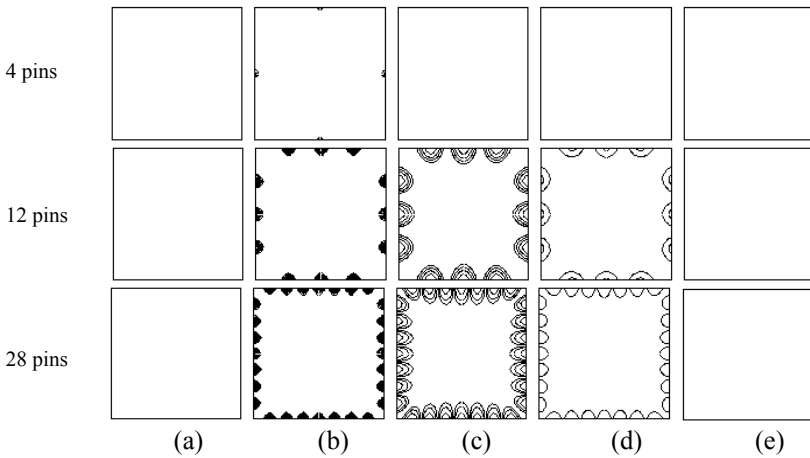


Fig. 8 Space charge distribution at various cross-sections, 24 kV, ( $\overline{\Delta\rho_c} = 0.05$ ) (a)  $\bar{z} = 1/4$ ; (b)  $\bar{z} = 1/2$ ; (c)  $\bar{z} = 11/16$ ; (d)  $\bar{z} = 7/8$ ; (e)  $\bar{z} = 1$ .

sents the channel width, with  $x = 0$  and  $x = 4$  referring to the channel walls. The experimental uncertainty is shown as an error bar along with the data. As seen from the figure, at a low voltage ( $V_0 = 20$  kV), the velocity profile appears uniform and there is good agreement between the experimental results and numerical simulations. As the applied voltage increases to 24 kV, velocities from the numerical simulation are still in the range of experimental uncertainty except for the location at  $x = 3$  in. It is suspected that the probe of the velocity transducer may have affected the flow measurement due to its insertion. The velocity profile at this applied voltage is still considered uniform across the channel. When the applied voltage is further increased to 28 kV, the discrepancy between the experimental results and numerical predictions becomes more obvious. Nevertheless, they both show an inverted parabolic profile with the maximum velocities occurring near the walls. This unique velocity profile reveals that the corona wind issued from the electrode pins behaves like a wall jet, disrupting the development of boundary layer.

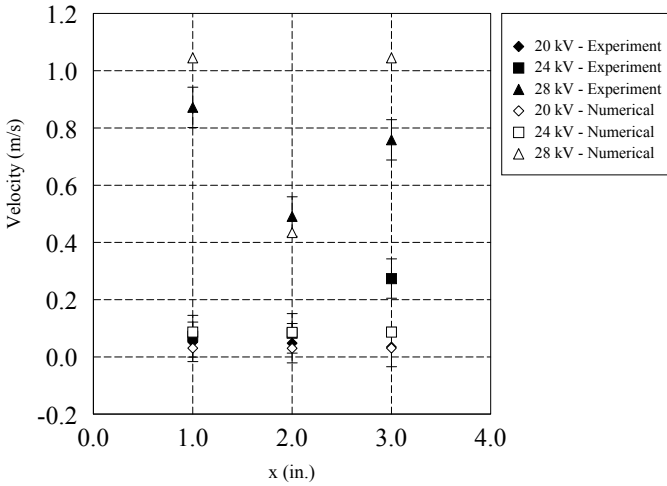


Fig. 9 Comparison of velocity profiles for the configuration with 12 electrode pins.

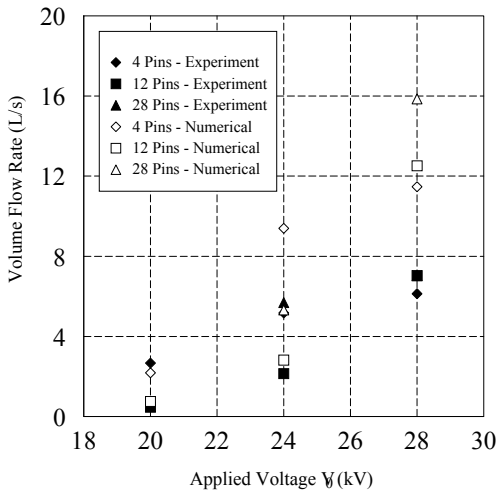


Fig. 10 Comparison of volume flow rate (positive corona discharge)

The non-symmetric velocity profile from the experiment is another indication of the interference caused by the presence of the velocity probe.

Figure 10 shows the volume flow rate produced by the three EHD gas pumps considered. As seen from the figure, at a low applied voltage ( $V_0 = 20$  kV), the agreement between the experimental results and numerical simulations is quite good for configurations with 4 pins and 12 pins. The configuration with 28 pins does not produce any detectable volume flow rate at the applied voltage of 20 kV since its corona onset voltage is about 21 kV. When the applied voltage is increased to 24 kV, good agreement can still be found between the experimental and numerical results except for the configuration with 4 pins. At a higher voltage ( $V_0 = 28$  kV), the experimental results are all smaller than the

numerical predictions. The discrepancy can be attributed to the limited number of velocity measurement points in experiment. Particularly, at a higher voltage, the induced air velocity becomes quite large close to the wall which is not well accounted for. Despite of some discrepancies, numerical results display the same trend as that of experiments, that is, the volume flow rate increases with an increase in the applied voltage for all configuration.

From the numerical results obtained, one can also get a better insight to the flow field developed in the channel. For example, this is presented in Fig. 11 for the EHD gas pump with 12 electrode pins. It is clearly seen that the high velocities occur around the electrode pins where the electric field is most intense. Meanwhile, flow with a lower velocity is confined to the corners of the channel. With an applied voltage of 28 kV, the maximum velocity inside the channel is about 5 m/s. This EHD gas pump induces a fairly uniform flow with a magnitude of 1 m/s at the top inlet of the channel.

To better understand the flow characteristics, the velocity contours at various cross-sections inside the channel are shown in Fig. 12. In the figure shown, cross-section (a) is located at the level of the electrode wire loop ( $\bar{z} = 1/4$ ). Cross-section (b) is located at the level of the electrode tips ( $\bar{z} = 1/2$ ). Cross-section (c) is located half-way between the electrode tips and the grounded plate ( $\bar{z} = 3/4$ ). Cross-section (d) is aligned with the bottom edge of the grounded plate ( $\bar{z} = 1$ ). Both two-dimensional and three-dimensional views of the velocity contours are shown at each cross-section. The magnitude of the velocity can be identified from the color scale shown in the legend. As observed, the velocity is rather uniform at the electrode wire loop level (Fig. 12(a)). Downstream the corona wind effect becomes visible. The three-dimensional contours clearly show that the corona wind issued from the electrode tip behaves like a wall jet, producing high velocity gradient near the channel wall while a relatively uniform velocity in the center (Fig. 12(b)). Although the highest charge density occurs at the wire tips, the highest velocity occurs below the wire tips (Fig. 12(c)-(d)). While the corona wind continues to develop downwards, it also extends towards the center of the channel. The visualization of three-dimensional flow profiles from the numerical simulations has provided firm

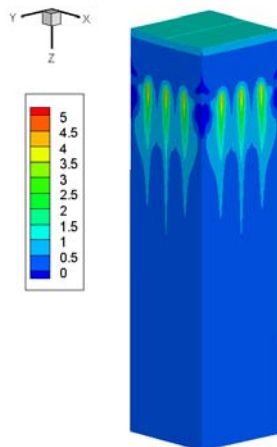


Fig. 11 Flow field induced by an EHD gas pump with 12 pins at  $V_0 = 28$  kV.

support for the experimental data in Fig. 9.

To evaluate the performance of EHD gas pumps against conventional fans, an energy efficiency rating is employed, which is defined as the amount of air delivered per unit of electric power used. The unit for this rating is usually CFM/W (cubic feet per minute per watt) or L/s/W (liters per second per watt).

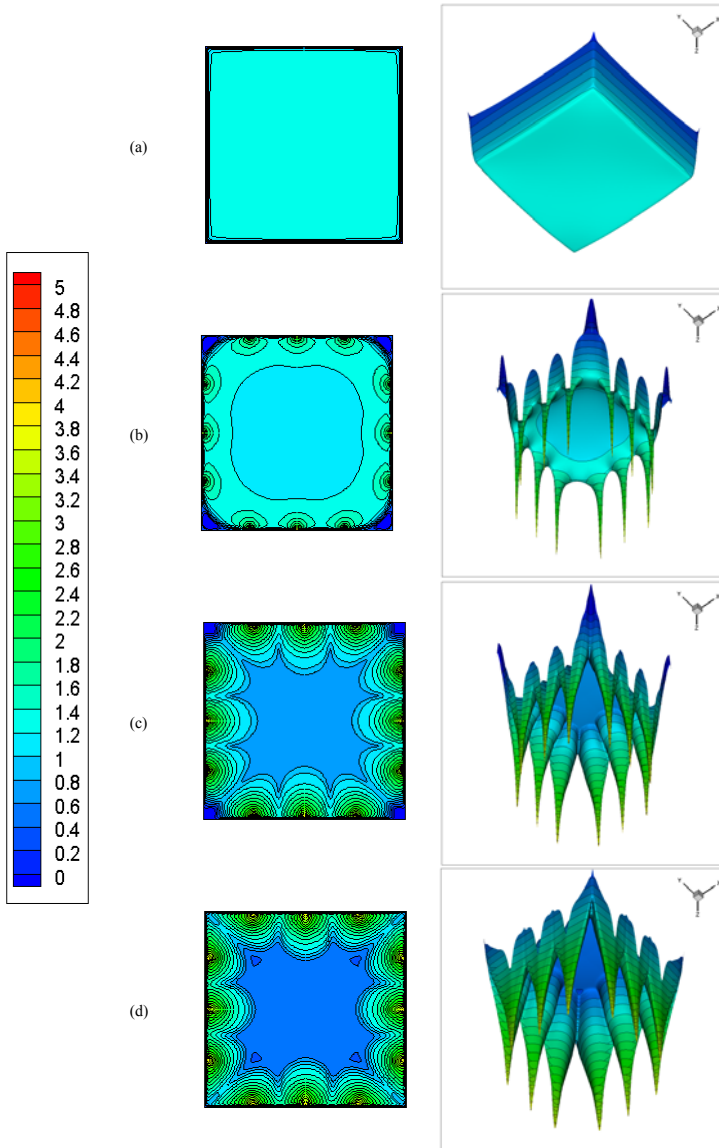


Fig. 12 Cross-sectional views of flow field induced by an EHD gas pump with 12 pins at  $V_0 = 28$  kV (a)  $\bar{z} = 1/4$ , (b)  $\bar{z} = 1/2$ , (c)  $\bar{z} = 3/4$ , (d)  $\bar{z} = 1$ .

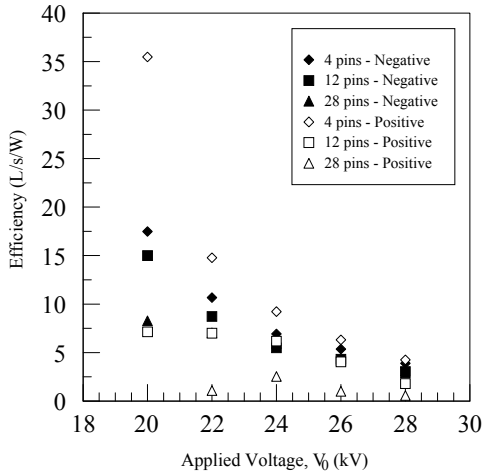


Fig. 13 EHD gas pump performance as a function of applied voltage.

Table 1. Performance of Conventional Cooling Fans for Personal Computer [19]

Conventional Cooling Fans	Fan Diameter (mm)	Performance (L/s/W)
Pentium II in desktop chassis	40	1.79
Pentium II & III in tower chassis	50	3.15
Pentium III in 1U server chassis	50	3.67
Pentium 4 in 1U server chassis	60	2.31

Figure 13 shows the EHD gas pump performance as a function of the applied voltage for three electrode configurations considered. The gas pump has a maximum performance of 35 L/s/W for the configuration with 4 electrode pins operated at an applied voltage of 20 kV with positive corona discharge. The performance decreases as the applied voltage increases. It is observed that the configuration with a fewer number of electrode pins has a higher efficiency rating. No definite conclusion can be drawn about the effect of polarity on the performance.

The performance of conventional computer fans ranges from 1 to 4 L/s/W as shown in Table 1 [19], which is considered low when comparing with those shown in Fig. 13. Thus the EHD gas pump proposed in the present study has a higher efficiency in energy usage. In addition, with no moving parts, the EHD gas pump offers much quieter operation than the conventional fans.

## CONCLUSION

Experimental and numerical studies have been conducted on an EHD gas pump with three electrode configurations (4 pins, 12 pins, and 28 pins) operated by either positive or negative DC voltage. It has been shown that the induced air velocity increases with an increase in the applied voltage. The velocity profile inside the channel reveals that the

corona wind issuing from the electrodes accelerates the air flow near the wall, resulting in a reversed parabolic velocity profile in the center of the channel. At a lower applied voltage ( $V_0 \leq 24$  kV), negative corona produces higher velocity and volume flow rate than positive corona. However, this trend is reversed at a higher applied voltage ( $V_0 > 24$  kV). The EHD gas pump with 4 electrode pins induces more air flow than those with 12 or 28 pins at low applied voltages. However, as the applied voltage increases, the configurations with more electrode pins produce higher volume flow rates. The highest volume flow rate of air produced by the EHD pump is as high as 7 liters per second for the configuration of 28 electrode pins with positive discharge. For performance, it has been shown that the EHD gas pump proposed is more effective than most conventional fans. Depending on the application, the present EHD pump can be further tailored (in terms of electrode configuration and applied voltage) to achieve the desired outcome.

#### NOMENCLATURE

b	ion mobility of air
D	channel width
$E_x$	electric field strength in x-direction
$E_y$	electric field strength in y-direction
$E_z$	electric field strength in z-direction
$I_{cal}$	numerically calculated corona current
$I_{exp}$	experimentally measured corona current
L	length of channel
p	pressure
u	velocity in x-direction
v	velocity in y-direction
V	electric potential
$V_0$	applied voltage at the wire
$\bar{V}$	normalized electric potential, $= V/V_0$
w	velocity in z-direction
W	width of the grounded plate
x, y, z	Cartesian coordinates
$\bar{z}$	normalized channel length, $z/D$
$\epsilon$	permittivity of air
$\rho_c$	space charge
$\rho_{c0}$	space charge at the wire tip
$\bar{\rho}_c$	normalized space charge, $= \rho_c/\rho_{c0}$

#### REFERENCES

- [1] T. B. Jones, Electrohydrodynamically Enhanced Heat Transfer in Liquids – A Review, *Advances in Heat Transfer*, vol. 14, pp. 107-148, Academic Press, New York, 1978.
- [2] J. H. Davidson, F. A. Kulacki and P. F. Dunn, Convective Heat Transfer with Electric and Magnetic Fields, *Handbook of Single-Phase Convective Heat Transfer*, edited by Kakac, S., et al., Wiley, New York, 1987.
- [3] J. Seyed-Yagoobi and J. E. Bryan, Enhancement of Heat Transfer and Mass Transport in Single-Phase and Two-Phase Flows with Electrohydrodynamics, *Advances in Heat Transfer*, vol. 33, pp. 95-186, 1999.
- [4] J. Seyed-Yagoobi, Electrohydrodynamic Pumping of Dielectric Liquids, *Journal of Electrostatics*, vol. 63, pp. 861-869, 2005.

- [5] M. Rickard, D. Dunn-Rankin, F. Weinberg, and F. Carleton, Characterization of Ionic Wind Velocity, *Journal of Electrostatics*, vol. 63, pp. 711-716, 2005.
- [6] H. Tsubonea, J. Ueno, B. Komeili, S. Minami, G. D. Harvel, K. Urashima, C. Y. Ching, and J. S. Chang, Flow Characteristics of Wire-non-parallel Plate Electrohydrodynamic Gas Pumps, *Journal of Electrostatics*, vol. 66, pp. 115-121, 2008.
- [7] J. S. Chang, H. Tsubone, Y. N. Chun, A. A. Berezin, and K. Urashima, Mechanism of Electrohydrodynamically Induced Flow in a Wire-non-parallel Plate Electrode Type Gas Pump, *Journal of Electrostatics*, vol. 67, pp. 335-339, 2009.
- [8] B. Komeili, J. S. Chang, G. D. Harvel, C. Y. Ching, and D. Brocilo, Flow Characteristics of Wire-rod Type Electrohydrodynamic Gas Pump under Negative Corona Operations, *Journal of Electrostatics*, vol. 66, pp. 342-353, 2008.
- [9] E. Moreau and G. Touchard, Enhancing the Mechanical Efficiency of Electric Wind in Corona Discharges, *Journal of Electrostatics*, vol. 66, pp. 39-44, 2008.
- [10] A. Shooshtari, M. Ohadi, and F. Franca, Experimental and Numerical Analysis of Electrohydrodynamic Enhancement of Heat Transfer in Air Laminar Channel Flow, *19th IEEE SEMI-THERM Symposium*, pp. 48-52, 2003.
- [11] D. J. Laser and J. G. Santiago, A Review of Micropumps, *Journal of Micromechanics and Microengineering*, vol. 14, pp. R35-R64, 2004.
- [12] J. Zhang and F. C. Lai, Electric Field in a Rectangular Channel with an Electrohydrodynamic Gas Pump, *Proceedings of the Electrostatics Society of America (ESA) Annual Meeting on Electrostatics 2008, Paper E2*.
- [13] T. Yamamoto and H. R. Velkoff, "Electrohydrodynamics in an Electrostatic Precipitator," *Journal of Fluid Mechanics*, vol. 108, pp. 1-18, 1981.
- [14] J. R. McDonald, W. B. Smith, H. W. Spencer and L. E. Sparks, "A Mathematical Model for Calculating Electrical Conditions in Wire-Duct Electrostatic Precipitation Devices," *Journal of Applied Physics*, vol. 48, pp. 2231-2243, 1977.
- [15] G. A. Kallio and D. E. Stock, "Computation of Electrical Conditions Inside Wire-Duct Electrostatic Precipitators Using a Combined Finite-Element, Finite-Difference Technique," *Journal of Applied Physics*, vol. 59, pp. 999-1005, 1985.
- [16] F. W. Peek, *Dielectric Phenomenon in High Voltage Engineering*, McGraw-Hill, New York, 1966.
- [17] F. C. Lai, P. J. McKinney and J. H. Davidson, "Oscillatory Electrohydrodynamic Gas Flows," *Journal of Fluids Engineering*, vol. 117, pp. 491-497, 1995.
- [18] F. C. Lai and S. S. Kulkarni, "Effects of Buoyancy on EHD-Enhanced Forced Convection in a Vertical Channel," *Journal of Thermophysics and Heat Transfer*, vol. 21, pp. 730-735, 2007.
- [19] N. E. Jewell-Larsen, I. A. Krichtafovitch, and A. V. Mamishev, "Design and Optimization of Electrostatic Fluid Accelerators," *IEEE Transactions on Dielectrics and Electrical Insulation*, vol. 13, pp. 191-203, 2006.